FULL PAPER

A systematic scheme to develop dynamic earthquake rupture scenarios: a case study on the Wenchuan–Maoxian Fault in the Longmen Shan, China, thrust belt

Rongjiang Tang[1]* and Ryosuke Ando[2]

Abstract

The 2008 Wenchuan Mw 7.9 mainshock caused catastrophic destruction to cities along the northwestern margin of the Sichuan Basin. This earthquake did not activate the Wenchuan–Maoxian Fault (WMF) on the hinterland side and the conjugate buried Lixian Fault (LXF), but they could experience large earthquakes in the future. We propose a systematic scheme to develop scenario earthquakes for active fault systems with insufficient constrain of 3D fault geometries. We first performed stress tensor inversion to constrain the regional stress field. Then, we developed a new method to constrain fault geometries by inverting long-term slip rates under the given regional stress and applied it to the WMF. We conducted a set of 3D dynamic earthquake rupture simulations on the WMF and LXF to assess the scenarios of earthquake rupture processes. Several fault nucleation points, friction coefficients, and initial stress states are assessed, the general rupture patterns for these earthquake scenarios are evaluated, and finally, we find the scenarios that could fall into three groups. Depending on initial conditions, the dynamic rupture may start in the LXF, leading to magnitude-7.0 earthquakes, or start in the WMF, then cascade through the LXF, leading to magnitude-7.5 earthquakes, or both start and arrest in the WMF, leading to around magnitude-6.5 or -7.0 earthquakes. We find that the rupture starting on the reverse oblique-slip jumps to the strike-slip fault, but the reverse process is impeded.

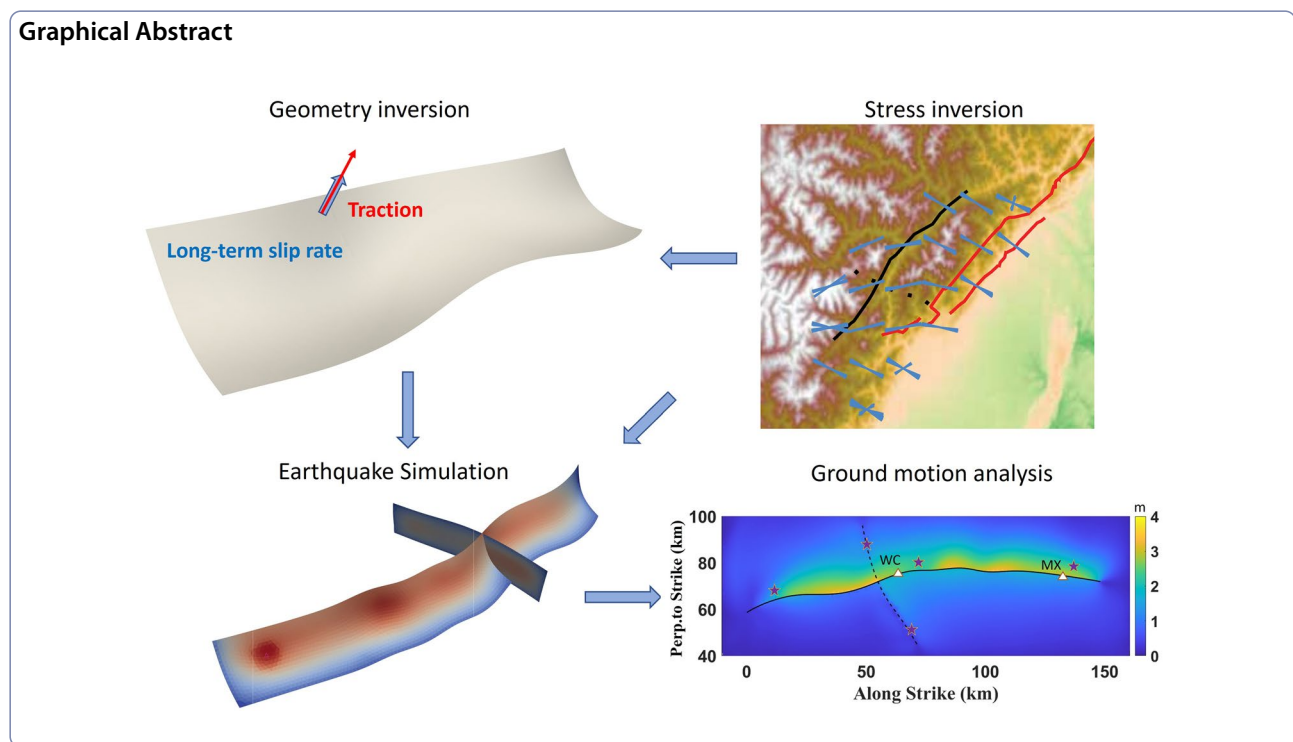**Keywords** Wenchuan–Maoxian Fault, Dynamic simulation, Fault geometry inversion, Strong ground motion

*Correspondence:
Rongjiang Tang
rongjiang.igp@hotmail.com
Full list of author information is available at the end of the article

Graphical Abstract

Geometry inversion

Stress inversion

Earthquake Simulation

Ground motion analysis

Introduction

The 2008 Mw7.9 Wenchuan earthquake caused devastating destruction to cities and counties along the active faults of the Longmen Shan thrust belt. Three parallel NW-dipping fault zones from the hinterland to the foreland [the Wenchuan–Maoxian Fault (WMF), the Beichuan Fault (BCF), and the Pengguan Fault (PGF)] constitute the crustal structure of the Longmen Shan Fault Zone (LMSFZ) (Fig. 1). The mainshock and aftershocks only ruptured the BCF and PGF (Xu et al. 2009; Feng et al. 2017; Liu-Zeng et al. 2009). Several counties, including Yingxiu, Beichuan, and Nanba, suffered a disaster in this event. One reason is that the fault almost passes through the center of these counties (Fig. 1). Similarly, the WMF also passes through the urban areas of Wenchuan, Maoxian, and several towns. Nearly 200,000 inhabitants live in the area along this fault. Should an earthquake in the future occur on the WMF, it would cause a significant hazard to densely populated towns. Assessing earthquake rupture scenarios in the future is essential to increase society's preparedness.

Dynamic rupture simulations intrinsically simulate physically self-consistent features of earthquake behavior and reproduce retrospectively large earthquake events (Aochi and Fukuyama 2002; Ando et al. 2017; Ando and Kaneko 2018; Ulrich et al. 2019). Since the dynamic rupture simulation is a forward problem to constrain the model based on the pre-seismic observations, efforts are

made to use it to explore future scenario earthquakes under pre-seismic estimation of stress conditions and fault geometries (Oglesby and Mai 2012; Zhang et al. 2017; Aochi and Ulrich 2015; Ramos et al. 2021; Harris et al. 2021; Yao and Yang 2022).

Three-dimensional fault geometry is a dominant factor in earthquake rupture dynamics. Irregular fault geometry, such as bends, branches, intersections, and stepovers, have been evidenced to cause rupture initiation and termination (Oglesby 2005; Elliott et al. 2015; Yang et al. 2013; Ando and Kaneko 2018). Several studies (Shi et al. 1998; Oglesby et al. 2000; Ma and Beroza 2008; Tang et al. 2021a) have shown that the dip angle, which leads to the asymmetric geometry of dip-slip or oblique faults intersecting the free surface, can affect the dynamics of earthquake rupture and ground motions considerably. In earthquake simulations, fault geometry is typically obtained from detailed relocation of aftershocks (Wu et al. 2009; Zhao et al. 2011; Yin et al. 2018), inversions using interferometric synthetic aperture radar (InSAR) measurements (Shen et al. 2009; Wan et al. 2016; Fukahata and Hashimoto 2016) and seismic reflection data (Hubbard et al. 2010; Jia et al. 2010; Lu et al. 2014). These methods are only available to investigate earthquakes that have already occurred. Seismic reflection and borehole surveys can estimate pre-seismic estimates of fault geometry, but they are costly in operations, and the data are not always available. Additionally, gravity and magnetic
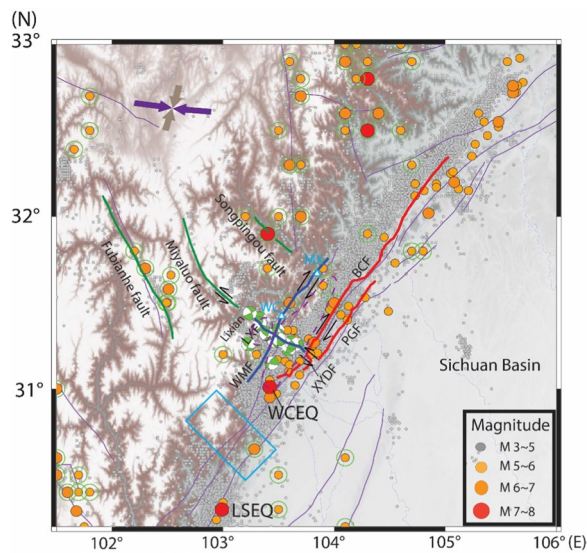
Fig. 1 Map showing the setting of major faults of the center Longmen Shan fault zone. The red bold lines indicate the field-confirmed rupture traces in the Wenchuan earthquake (Xu et al. 2009; Liu-Zeng et al. 2009). The blue solid lines represent the WMF and LXF, both of which did not slip in the mainshock but are very active in aftershocks. The green solid lines represent three active faults parallel to the LXF. Accurate fault trace of the WMF is derived from field investigation of Xie et al (2011), and the location of the LXF trace is deduced from the distribution of pure strike-slip aftershocks (Li et al. 2019). Historical earthquake catalog denoted by filled circles refers to Wang et al (2021) and China Earthquake Networks Center (http://data.earthquake.cn). Green hollow circles denote the historic strong earthquakes (M > 5) before 2008 Wenchuan event. The purple and gray coupled arrows depict the maximum and minimum horizontal compressional stress fields (Luna and Hetland 2013). The third primary stress (not shown) is vertical. The purple dashed regions, respectively, show the positions of Xuelongbao (north) and Pengguan (south) Massif (Shen et al. 2019). The blue box shows the seismic gap near Dayi town. WC—Wenchuan. MX—Maoxian. WMF—Wenchuan Maoxian Fault. LXF—Lixian Fault. BCF—Beichuan Fault. PGF—Pengguan Fault. XYDF—Xiaoyudong Fault. WCEQ—Wenchuan Earthquake. LSEQ—Lushan Earthquake

Moreover, this hypothesis is confirmed based on a large natural earthquake's seismically inverted slip distributions (Matsumoto et al. 2018). Recent detailed analyses of InSAR observations demonstrate that the slip direction at the ground surface is consistent with those of the overall characteristics at seismogenic depths (Fukahata and Hashimoto 2016). Therefore, in an ideal case, the fault plane and the principal stresses should uniquely determine the sense and direction of the long-term slip rate. Since geological and geomorphological observations can determine fault strikes, principal stress axes, and long-term slip rates, the Wallace–Bott hypothesis suggests that dip angles can be inferred based on these observations. In fact, this idea is a natural and quantitative extension of our commonly used experience to distinguish the near-vertical strike-slip faults from more tilted dip-slip faults. An advantage of this method is that we can provide observation-based and systematic inferences of the fault geometry even if more direct data such as seismic reflections survey and hypocenter locations are absent.

In this study, we first calculate the distribution of heterogeneous stress fields near the WMF based on the focal mechanism solutions (FMS) of 2008 Wenchuan earthquake aftershocks ($M \geq 3.5$). The heterogeneous on-fault initial stresses are resolved from the tectonic stress tensors. Then, we use the long-term slip rate together with the inferred stress to refine the WMF structure based on the Wallace–Bott hypothesis. We then implemented dynamic rupture simulations to investigate rupture propagations on the WMF and surrounding faults to assess potential rupture scenarios.

(Tian et al. 2017), seismic tomography (Tong et al. 2019), and magnetotelluric sounding (Zhao et al. 2012) cannot provide enough spatial resolution to describe the fault geometry, especially the dip angles. More straightforward and more effective methods have been awaited.

We propose a new method to infer the fault geometry by inverting the long-term slip rate based on the Wallace–Bott hypothesis (Wallace 1951; Bott 1959) to refine the fault geometry based on the existing inference of the WMF (Hubbard et al. 2010) and the surface fault trace (Xie et al. 2011). This hypothesis recalls that two bodies in contact slip toward the interfacial tangential traction and asserts that faults slip in the same manner (Fig. 2). This is also the base of the widely used stress tensor inversion method (Hardebeck and Michael 2006).
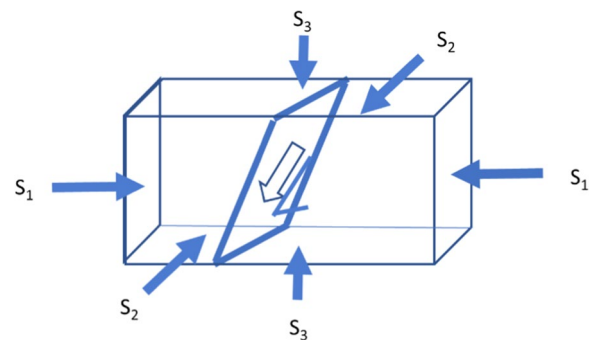

Fig. 2 Wallace–Bott hypothesis. Two bodies contacted through the surface (fault) are subjected to the principal stresses S_1, S_2, and S_3 and the projection of them gives the on-fault tangential traction, which is oriented in the direction shown by open arrow. The slip occurs in the same direction (one-sided arrow indicates the motion of the lower plate)

Seismic and tectonic condition of the Wenchuan–Maoxian fault and Lixian fault

The WMF has prominent fault orientation and geometry similarities to the BCF and PGF that caused the 2008 mainshock. The three faults are subparallel and horizontally spaced within 20 km (Fig. 1) and might root into the same main detachment with a depth of approximately 20 km. The main fault shapes display a classic ramp-flat geometry (Hubbard et al. 2010; Jia et al. 2010; Li et al. 2010). Tang et al.'s (2021b) simulation revealed that the Wenchuan mainshock changed the stress on the WMF, generating a positive Coulomb-failure stress change (ΔCFS) in the center portion of the WMF, suggesting that the 2008 mainshock might have clock-advanced the next earthquake on the WMF to some extent. The WMF has not experienced a strong earthquake for more than 300 years since the last M-6.5 earthquake in 1657 (National Earthquake Data Center, http://data.earthquake.cn), and the current earthquake interval might provide sufficient accumulated strain for a moderate earthquake ($5.5 < M < 6.5$) (Additional file 1: Fig. S1).

Field studies show that the WMF primarily exhibited dextral strike-slip faulting with a comparable reverse component (Tang 1991; Rongjun et al. 2007; Shen et al. 2019; Tian et al. 2013; Tan et al. 2017) since the Late Cenozoic, consistent with the coseismic slip sense and the long-term slip rate of BCF and PGF (Rongjun et al. 2007; Densmore et al. 2007; Xu et al. 2009; Liu-Zeng et al. 2009; Feng et al. 2017). Based on fission track and (U–Th)/He dating, Shen et al. (2019) obtained a 0.6 mm/yr long-term slip rate of WMF, which is as high as those along the frontal BCF (~ 0.54 mm/yr before the Wenchuan earthquake (Rongjun et al. 2007) and 0.88–0.91 mm/yr after the Wenchuan event (Ran et al. 2013)].

In addition, according to observational seismic records before the Wenchuan earthquake (Additional file 1: Fig. S1), four earthquakes occurred near the WMF out of 11 moderate earthquakes ($5 < M < 6$) in this area. Note that 12 Ms > 5.6 aftershocks occurred within 1 year after the 2008 Wenchuan earthquake, of which one Ms 6.1 event occurred on the southernmost end of the WMF and one Ms 6.0 event in the Lixian Fault (LXF) (Zhao et al. 2011).

The buried LXF is geometrically close to the WMF and bridges between the WMF and the BCF by its conjugate geometry (Fig. 1), which may result in cascading ruptures to form larger earthquakes. Geological studies are scant, and the activity is yet to be clarified for this fault due to the heavy vegetation cover and rugged terrain. The maximum altitude difference exceeds 3 km (Tan et al. 2017). The LXF appears to extend to the Miyaluo Fault, a well-defined geological structure (Fig. 1) displaying a sinistral sense of slip with unknown slip rates and thought to be active at least during the Pleistocene based on the fission track dating (Yang and Zhang 2010). Several earthquakes larger than M-7 were recorded on the Fubianhe and Songpinggou Faults, which are subparallel to the Miyaluo Fault with an NW strike orientation (Fig. 1). In the following section of the stress inversion analysis, the LXF exhibits the most favorable orientation in the regional stress field. Therefore, the LXF might display a comparatively high seismic potential, although none of the great earthquakes has been recorded to have occurred on it recently.

Regional stress inversion and modeling

The initial stress conditions are fundamental in controlling dynamic earthquake rupture processes (Harris 2004; Ramos et al. 2022). We inferred the present regional tectonic stress field by inverting earthquake
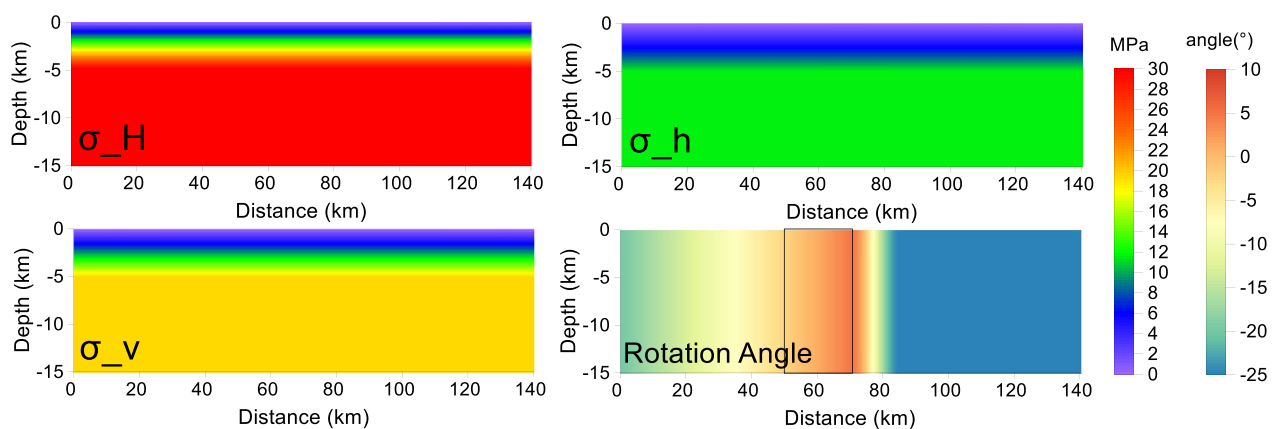

Fig. 3 Along strike distribution of three-component principal stress (σ_H, σ_h for the maximum and minimum horizontal principal stresses, and σ_v for vertical principal stresses). The lower right figure shows the angle between the east and the maximum horizontal stress axis (negative denotes the clockwise), and black box denotes the projection of LXF

FMSs (from Li et al. 2019) of 2008 Wenchuan earthquake aftershocks for computationally simulating earthquake scenarios in this region. We adopted a damped linear stress inversion method developed by Hardebeck and Michael (2006) to determine the stress field using FMSs. This method enables us to infer the directions of the principal stresses σ_r ($r = 1, 2,$ and 3 for the maximum, intermediate, and minimum principal stresses, respectively) and the ratio between the principal stresses σ_r, defined as $\varnothing = (\sigma_2 - \sigma_3)/(\sigma_1 - \sigma_2)$. The details of the method and results are described in Additional file 1: Text S1.

However, in our dynamic rupture simulation, these observationally constrained parameters are insufficient to determine the absolute values of the principal stresses. Two unknowns are needed and obtained by imposing other prior information. For simplification, we first assume that one of the principal stress axes is vertical based on the observation near the WMF, as by Anderson (1905). Then, we constrain σ_H/σ_v to 1.6, an approximate value from the in situ stress measurements along the BCF after the Wenchuan earthquake (Qin et al. 2015) and previous simulation works (Duan 2010; Zhang et al. 2019; Tang et al. 2021b), where σ_H and σ_v denote the magnitudes of the maximum horizontal and vertical principal stresses. The σ_H along the depth is constrained by assuming that the average stress drop satisfies the stress drop derived from empirical relations (Kanamori and Anderson 1975). We assume typical overburden stress and that the pore pressure increases with the depth, and the latter gradient gradually approaches the former (Rice 1992), so that the stress is tapered to the ambient value at a specific depth (here, we set 5 km) (Rice 1993). Figure 3 shows the resulting stress field model of the WMF. The along-strike rotation of the principal horizontal stresses reflects our inversion result. Since there are no independent constraints on the specific depth of the WMF, we discuss its influence in the section "Effect of saturation depth of stress".

Fault geometry construction

Our dynamic model must match the observed oblique dextral slip WMF and the almost pure sinistral strike-slip LXF in the long-term slip rate. We set the LXF as vertical, with a 0.5 km buried depth and a 15 km basal depth inferred from the average seismogenic depth (Shen et al. 2009; Wan et al. 2016; Ramirez-Guzman and Hartzell 2020). In the simulation, we model only the southern portion of the LXF, and do not consider its possible extent further to the north, which could be hypothetically a link to the Miyaluo Fault (Yang and Zhang 2010).

The aftershocks of the M-7.9 Wenchuan earthquake and the 2013 M-7.0 Lushan earthquake delineated a prominent seismic gap approximately 50 km long near the town of Dayi (the blue box in Fig. 1). Several studies suggest that this gap can correspond to a possible unruptured fault segment (Wang et al. 2015, 2018; Liu et al. 2018), and, in this study, we assume that the south part of the WMF terminates near this gap.

Although we could mimic this fault system with several planar rectangular fault segments, we developed a nonplanar fault model by considering existing data and geological inferences. We developed the WMF geometry model by considering (1) geological investigations and seismic reflection data (Xu et al. 2009; Hubbard et al. 2010; Jia et al. 2010), providing an approximate geometry of the WMF at a depth: a fault subparallel to the BCF, with a larger dip angle and listric geometry. (2) The surface fault trace from field investigations (Xie et al. 2011) provides along-strike constraints on the surface fault structure. (3) The early aftershock locations (Yin et al. 2018) help constrain the south section of the WMF geometry. Based on these constraints, we refine the geometry by developing a new method by inverting the long-term slip rate and the regional stress field based on the above consistency between the slip direction and the tangential traction (Wallace–Bott hypothesis) (Fig. 2). The direction of the on-fault tangential traction is fully determined from the stress tensor inversion analysis, including the orientations of the three principal stress axes and the ratio between the magnitudes of the principal stresses (stress ratio) (Michael 1984). The validity of this new method is observationally supported by Matsumoto et al (2018); in the case of the 2016 M7.0 Kumamoto, Japan, earthquake, they demonstrated the good coincidence of the directions between the coseismic slip
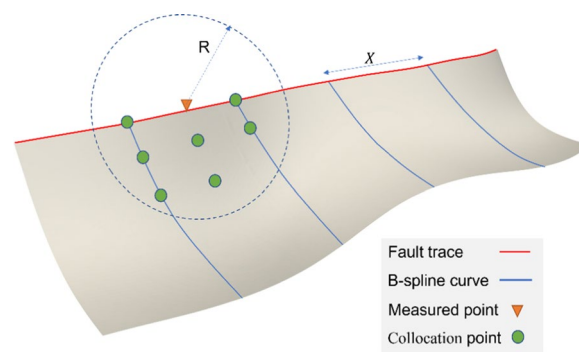

Fig. 4 Schematic to describe how the fault geometry is related to traction at measured points. We get the strike and dip angles for each collocation point using cubic spline interpolation (McKinley and Levine 1998), and the traction on each collocation point can be calculated through resolving the heterogeneous tectonic stress tensor along the fault strike and dip. Then, we get the averaged traction from all collocation points in the spherical computational region with radius R

constrained by the seismic inversion (Asano and Iwata 2016) and the tangential traction on the observationally constrained dipping fault surface where the tangential traction is resolved from the principal stresses obtained by the stress tensor inversion.

The readers should not confound our inferring dip angles with the internal or optimal frictional angles determined by the frictional coefficient. The dip angle inferred in our method is independent of the friction coefficient. In other words, our method does not hypothesize that

Fig. 5 Map showing the measured points of long-term slip rate along the WMF. Each gray box contains the locations and long-term slip rates measured from different researchers. Dextral means dextral strike-slip rates and Up (NW) means vertical slip rates with northwestern block being hanging wall. The red and blue lines are the same with Fig. 1. The red stars denote the measured points of long-term slip rate. Gray circles represent aftershocks of the 2008 earthquake (Yin et al. 2018)

faults occur in the most optimal orientation and has the flexibility to apply to misoriented faults under the recent tectonic stress conditions. Our approach can be valid if the regional stress fields are stable over time to have the observed long-term slip rates. While the temporal stability of tectonic stress regime (or the absolute stress level, not the stress change) considered here is an issue that needs more intensive investigations, at least, it appears to be insensitive to individual occurrence of large earthquakes (i.e., Imanishi et al. 2012).
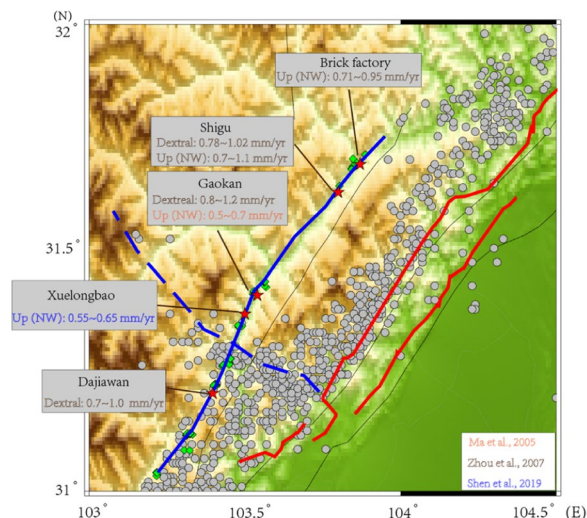
Geometry inversion method

A proper choice of geometry models should be made depending on purposes by considering the available data and previous inferences (Xu et al. 2009; Hubbard et al. 2010; Jia et al. 2010). A model of listric fault geometry is considered here by following the above models. The general dip angles are allowed to vary continuously along the fault strike, and the surface fault traces are fixed, as given by the data. We use one inversion parameter η to describe the fault dip in the local area by assuming the listric fault geometry, as described by (Wan et al. 2016)

$$z(y) = \frac{2h_0}{\pi}(y/\eta),\tag{1}$$

where z is the depth of the fault plane, and y is the horizontal distance of the fault plane from its surface trace. The fault surface is described by the B-spline varying continuously along the strike, with its downdip curvature dictated by the parameter η (Fig. 4). h_0 is the fault depth to invert and is assumed to be the same for all fault segments. n B-spline curves are uniformly distributed along the fault strike with equal horizontal intervals X to
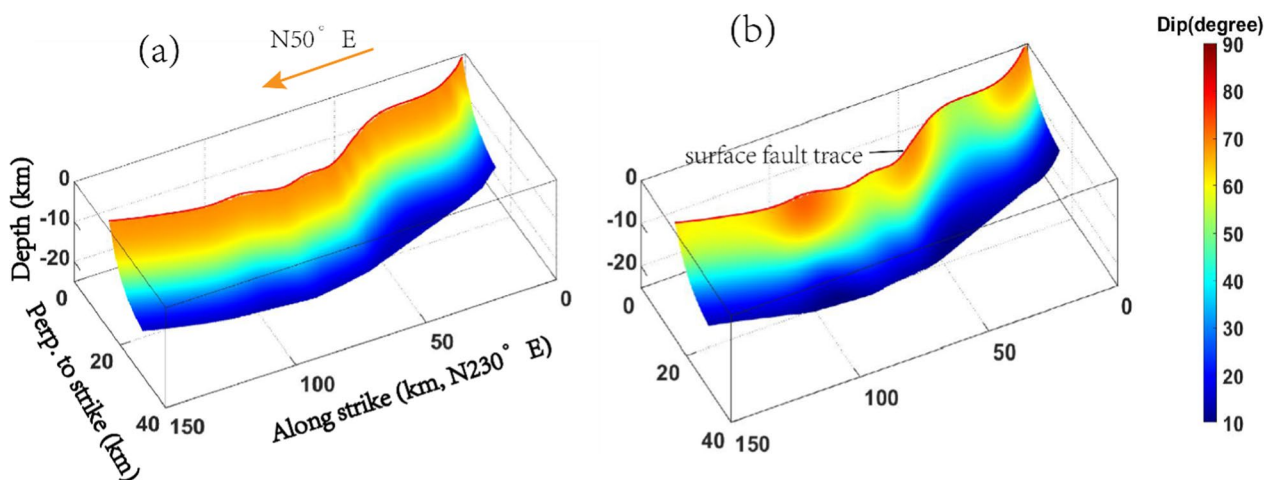

Fig. 6 Estimation of WMF geometry using 150 inversions. **a** Initial fault surface derived from the initial value of $\eta_0 = 5.0$, $h_0 = 18$ km. **b** Final fault surface derived from average η of 150 inversions

create the fault surface. Therefore, we have $n+1$ nonlinear model parameters to determine (i.e., n η values plus h_0)

$$\boldsymbol{m} = [\eta_1 \ldots \eta_n\, h_0]. \tag{2}$$

The direction of the long-term slip rate is approximately collinear with the traction on the fault plane, which is equivalent to solving the problem of minimizing the difference between the two ratios. We solve the inverse problem in the sense of Tikhonov (1963), taking a regularized solution to be a model minimizing an objective function, Ψ, defined by

$$\Psi(\boldsymbol{m}) = \|\frac{T_2(\boldsymbol{m})}{T_1(\boldsymbol{m}) + T_2(\boldsymbol{m})} - \frac{V_2}{V_1 + V_2}\|^2 + \lambda\|\boldsymbol{Lm}\|^2, \tag{3}$$
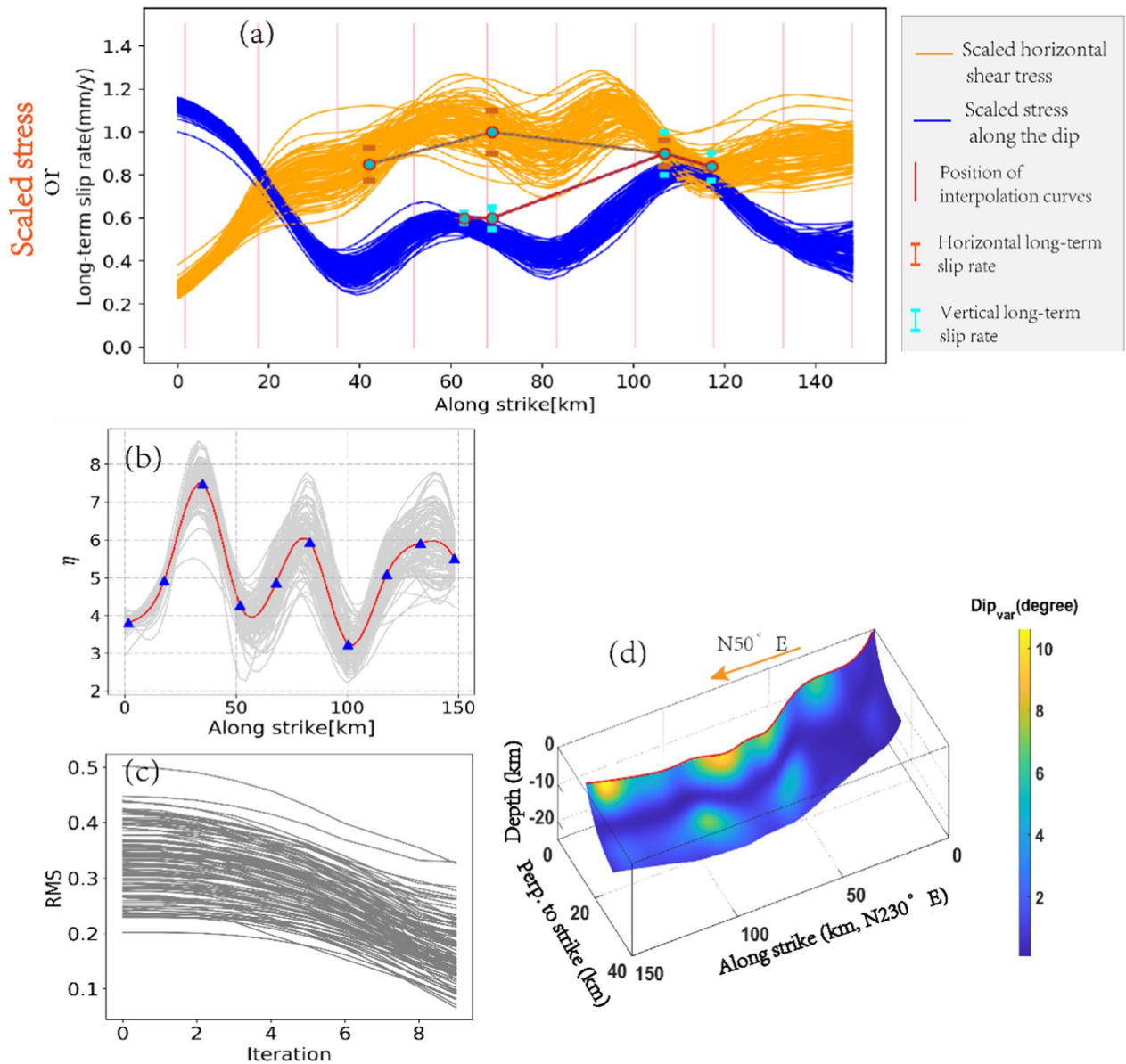

Fig. 7 Uncertainty of WMF geometry estimation. **a** Observed long-term slip rates and scaled traction. The blue and orange lines present weighted average shear stress along the dip and strike, respectively. The length of the bar indicates the standard deviation of slip rate. The vertical thin pink lines indicate the position of B-spline curves. **b** Distribution of inverted parameters τ, the red line is the average of 150 inversions (gray lines), and blue triangles indicate the position of interpolation curves. The average of inverted fault depth $h_0 = 16.11$ is not shown here. **c** Objective functions versus iterations from 100 inversions. **d** Standard variance distribution of fault dips derived from 150 inversions

where T_1 and T_2 denote the averaged traction along the strike and dip within each spherical computational region with radius R, respectively, represented at the measured points. The averaged traction introduced here can be regarded as a comprehensive effect within the computational region R and depends on the regional stress and fault geometry (Fig. 4). The V_1 and V_2 denote the horizontal and vertical long-term slip rates at the measured points. We choose the damping matrix **L** to be a simple, first-difference operator (make sense for only η not h). The regularization parameter λ is a positive number that balances the effects of data fitting and model smoothness, controlling the smoothness of model space.

However, the observed slip-rate ratios are not always obtained for each measured point, where either horizontal or vertical long-term slip rates can be given. We prefer to use an approximate form

$$
\begin{aligned}
\Psi(\boldsymbol{m}) = & \|\alpha \boldsymbol{T}_1(\boldsymbol{m}) - \boldsymbol{V}_1\|^2 \\
& + \|\alpha \boldsymbol{T}_2(\boldsymbol{m}) - \boldsymbol{V}_2\|^2 + \lambda \|\boldsymbol{L}\boldsymbol{m}\|^2,
\end{aligned}
\tag{4}
$$

where α is a scaled value manually set to meet the best initial misfit. We construct the forward model to connect the fault geometry parameters to weighted average tractions $T_1(\boldsymbol{m})$ and $T_2(\boldsymbol{m})$ near the surface (Fig. 4). We used the conjugate gradient method to obtain the optimal solution of $\boldsymbol{m}$. The forward calculation and inversion procedures were further elaborated in detail in Additional file: 1 Appendix A of the supplementary material.

Application to the WMF
In this study, the model parameter $\boldsymbol{m}$ include ten down-dip curvature parameters η uniformly distributed along the fault strike, plus h_0 for all curves. Under the condition that the values of η can accurately describe the surface trace and the nonplanar fault surface, we expect as few parameters as possible to avoid the overfitting problem due to limited observed data. We collected the vertical and horizontal components of the long-term slip rate from a few studies (Ma et al. 2005; Rongjun et al. 2007; Ran et al. 2013; Shen et al. 2019) shown in Fig. 5 and implemented five measured points with seven slip rates along the WMF in the inversion. We choose the B-spline interval X = 16 km, radius R = 15 km, and the update strategy of the regularization parameter λ based on the additional tests (Additional file 1: Text S2).

The long-term slip rate cannot be accurately measured due to the uncertainty of the geological age estimation of sediments (Rongjun et al. 2007; Shen et al. 2019). The inversion uncertainty is estimated using 100 bootstrap resamplings of the entire data set (seven slip rates) to obtain a more reliable result. The data from each measured point obey a Gaussian distribution.

For each inversion, we set the same initial model as $\boldsymbol{m} = [\eta_0, \ldots, \eta_0, h_0]$, where $\eta_0 = 5.0$, $h_0 = 18$ km (Fig. 6a). A few aftershocks are distributed at the south end of the WMF (Additional file 1: Fig. S2), which is helpful as prior information to constrain one of the inversion parameters. We can fit the aftershock distributions using Eq. (1) with $\eta_0 = 5.0$, $h_0 = 18$ km. Therefore, the parameter η at the southernmost position ($x = 0$ km) is enforced for little variation during the inversion.

An average of 100 inversions is derived to obtain the final fault model (Fig. 6b), where the dip angles near the surface vary along the fault strike due to the constraint of the observed long-term slip rates (Fig. 7a). The final inversion results are distributed in a narrow strand (Fig. 7b). All objective functions steadily decrease versus the iterations (Fig. 7c) and uncertainty of inverted dip angle is within 10° (Fig. 7d), justifying our method. The predicted average fault dip angles at the intersection of WMF and free surface are approximately 60°, typically larger than that in the southern section of the BCF. The above results are consistent with the previous studies (Xu et al. 2009; Hubbard et al. 2010; Jia et al. 2010). Differences in the dip angle can lead to differences in rupture scenarios, including the strong ground motion and surface offset for the BCF and WMF.

While we believe that this method of fault geometry inversion is an effective physically based and observationally supported tool, this method could involve ambiguities due to the limitations of the available data and model constraints in inversion analyses. Furthermore, the Wallace–Bott hypothesis is not always satisfied, as the slip direction might deviate from the tangential traction orientation by considering several factors, including local variation in fault geometry (Lejri et al. 2015; Lisle 2013). Nevertheless, we can find the utility of our optimized search method when we wish to refine previous models (Hubbard et al. 2010) or decide on a better model based on prior information without more direct geophysical or geological information.

Dynamic rupture simulation
Method
We computationally simulate spontaneous dynamic rupture propagation on the conjugate fault system of the WMF and LXF. The dynamic rupture problems are numerically solved by the Fast Domain Partitioning Boundary Integral Equation Method (FDP-BIEM) (Ando 2016; Ando et al. 2017; Ando and Kaneko 2018), which increases the efficiency of the elastodynamic boundary equation method (BIEM) without degradation in accuracy. We introduce additional 'free surface elements', on which a free surface boundary condition is satisfied (Ando and Okuyama 2010; Hok and Fukuyama 2011). This method could avoid further complicated theoretical
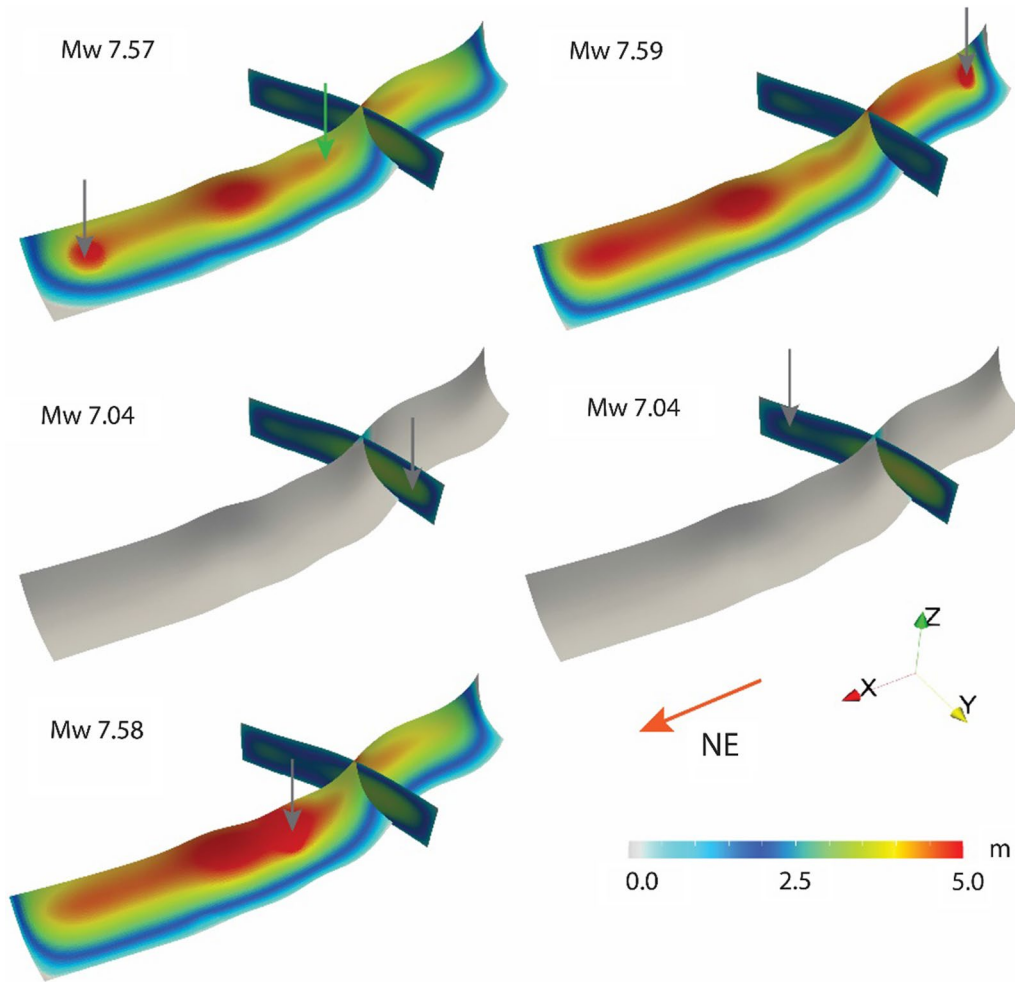
Fig. 8 Total slips and earthquake magnitudes from different nucleation points noted by gray arrows. The green arrow denotes the point in Fig. 13

computations for the integration kernels, and enable us to introduce rather complicated geometry of fault systems in a half-space medium. We consider a homogeneous elastic half-space, with Lamé parameters $\lambda = \mu = 28$ GPa and mass density $\rho = 2776$ kg/m³ ($v_p = 5500$ m/s, $v_s = 3175$ m/s). These parameters are based on the first-order approximation of a three-dimensional velocity structure around the Longmen Shan Fault obtained from seismic tomography (Pei et al. 2010; Wang et al. 2021). The local variation of shallow seismic velocity structures or site effects amplifying ground motion is excluded from this model. Instead, we focus on the source effect.

The boundary condition for the fault surface is considered where the frictional strength is described by the linear slip-weakening friction law (Andrews 1976)

$$\tau = \begin{cases} \left[\mu_s - (\mu_s - \mu_d)\frac{u}{D_c} \right]\sigma_n, u < D_c \\ \mu_d\sigma_n, u \ge D_c \end{cases}, \quad (5)$$

where D_c, μ_s, and μ_d denote the characteristic slip and the static and dynamic frictional coefficients, respectively. τ and σ_n represent the shear traction and normal stress, respectively. Based on the results of high-speed friction experiments (Yao et al. 2013), we set the friction coefficients uniformly on the entire fault with $\mu_s = 0.53$ and $\mu_d = 0.12$. We choose $D_c = 0.8$ m, because its upper bound is estimated to be 1.0–2.0 m by Tang et al. (2021b), who applied the approach proposed by Mikumo et al. (2003) to estimate the upper bound of D_c of the 2008 Wenchuan earthquake, constrained by the slip rates at fault locations from the kinematic inversion (Zhang et al. 2014) of near-field waveforms. The neighboring parameter space is also investigated and discussed in the section "Discussion", considering the uncertainties of these parameters. We first chose moderately low μ_s, μ_d, and D_c to allow the rupture to propagate to the artificially assumed boundaries without being arrested to explore large earthquake scenarios.

As for the numerical model size, we typically employed the boundary elements of approximately 26,824. We control triangular elements to be 500 m on the fault and free surface in the vicinity of the fault, and then increase this size with a maximum rate of 7.5 times toward the outer boundary of the free surface until it reaches the maximum size of around 2000 m, such that higher calculation accuracy can be achieved near the fault plane, and computational expense can be greatly reduced due to the gradual distribution of mesh density (Additional file 1: Fig. S3).

In the simulation, the ruptures are triggered by overstressing a small circle patch with a radius of 3 km , where the initial stress is uniform and slightly above the yield stress. Once a rupture is triggered, its subsequent development is controlled by the elastodynamic equation, the friction law, the initial stresses, as well as the fault geometry. Under our current state of knowledge, predicting a likely hypocenter on the fault system of the WMF and LXF is challenging. Therefore, we considered five nucleation locations at the center, the east and west ends of the WMF, and the north and south ends of the LXF. Considering stress changes caused by Wenchuan mainshock and aftershocks (Additional file 1: Text S3), we set one of the potential epicenters near the Wenchuan County.
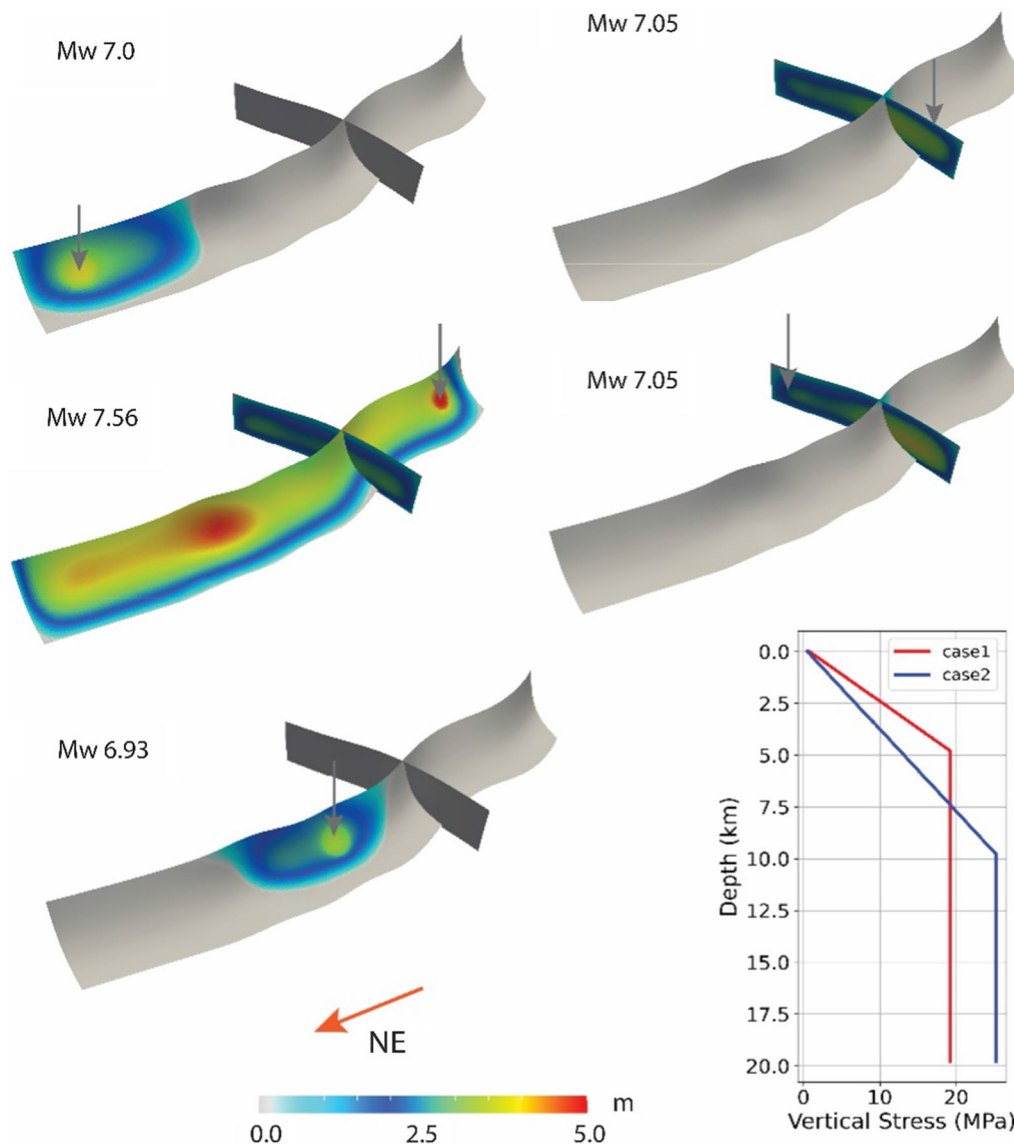

Fig. 9 Simulations (model E3 ~ C3 in Table 1) of the case 2 for depth-dependent vertical stress, the lower right sub-figure shows two different depth-dependent stress configurations with saturation depth 5 km and 10 km

Table 1 Models with a different set of friction and nucleation positions in this study

Model	μ_d	D_c (m)	H of σ_v* (km)	Depth of nucleation (km)	M_w	Arrest*	Dynamic triggering*	Total Seismic Moment (N m)
E1	0.12	0.8	5	6.5	7.57	No	Yes	2.893×10^{20}
W1	0.12	0.8	5	6.5	7.59	No	Yes	3.070×10^{20}
S1	0.12	0.8	5	6.5	7.04	No	No	4.686×10^{19}
N1	0.12	0.8	5	6.5	7.04	No	No	4.704×10^{19}
C1	0.12	0.8	5	6.5	7.58	No	No	3.048×10^{20}
E2	0.12	0.8	5	9.5	7.56	No	Yes	2.825×10^{20}
W2	0.12	0.8	5	9.5	7.59	No	Yes	3.060×10^{20}
E3	0.12	0.8	10	6.5	7.00	Yes	No	4.080×10^{19}
W3	0.12	0.8	10	6.5	7.56	No	Yes	2.823×10^{20}
N3	0.12	0.8	10	6.5	7.05	No	No	4.796×10^{19}
S3	0.12	0.8	10	6.5	7.05	No	No	4.774×10^{19}
C3	0.12	1.0	10	6.5	6.93	Yes	No	3.129×10^{19}
E4	0.15	0.8	5	6.5	6.92	Yes	No	3.118×10^{19}
W4	0.15	0.8	5	6.5	7.5	Yes	Yes	2.225×10^{20}
C4	0.15	0.8	5	6.5	7.42	Yes	Yes	1.703×10^{20}
W5	0.15	1.2	5	6.5	6.62	Yes	No	1.088×10^{19}
N5	0.15	1.2	5	6.5	7.00	No	No	4.109×10^{19}
S5	0.15	1.2	5	6.5	7.00	No	No	4.106×10^{19}
E5	0.15	1.2	5	6.5	6.65	Yes	No	1.207×10^{19}
C5	0.15	1.0	5	6.5	7.38	Yes	Yes	1.509×10^{20}

H of σ_v*: the saturation depth of the two different depth-dependent stress cases shown in Fig. 9

Arrest*: if Yes, the rupture will be arrested rather than reaching the assumed artificial barrier

Dynamic triggering*: if Yes, the rupture on one fault will trigger the secondary rupture on the other fault

The first letter of the model's name represents the nucleation location, and E1 ~ C1 have been elaborated in the result section

Results

Figure 8 shows the total slip distribution on the WMF and LXF and the moment magnitude for each case. The rupture tends to jump from the oblique-slip fault (in the WMF) to the strike-slip fault (in the LXF), but the reverse is more difficult. For instance, a dynamic rupture might start in the central, eastern, or western parts of the WMF, and then cascade to the LXF, leading to three comparable-sized earthquakes with M-7.56, M-7.55, or M-7.57. However, if it starts in the south or north of the LXF, triggering a second rupture on the WMF will be challenging (Fig. 8, video S1–S2), leading to a smaller earthquake with moment magnitudes 7.05 or 7.06.

The total slip on the LXF is smaller than that on the WMF. This might be surprising, because the stress drop

on the LXF is significantly larger than that on the WMF (Additional file 1: Fig. S4). Noting that the friction coefficients on the two faults are the same, and the faulting and geometry should cause the prominent difference between the coseismic slips. The WMF is a thrust fault with a larger extent in dip and strike than the LXF, which is a buried and smaller purely strike-slip fault. Under the same stress conditions, larger faults tend to slip more, because healing phases suppressing slip may arrive later, and the free-surface effect is reduced for buried faults. Numerical simulations show that thrust faults have larger coseismic slips than normal and strike-slip faults (Oglesby et al. 2000; Tang et al. 2021a) named the hanging wall effect (Abrahamson and Somerville 1996), because the reflected waves from
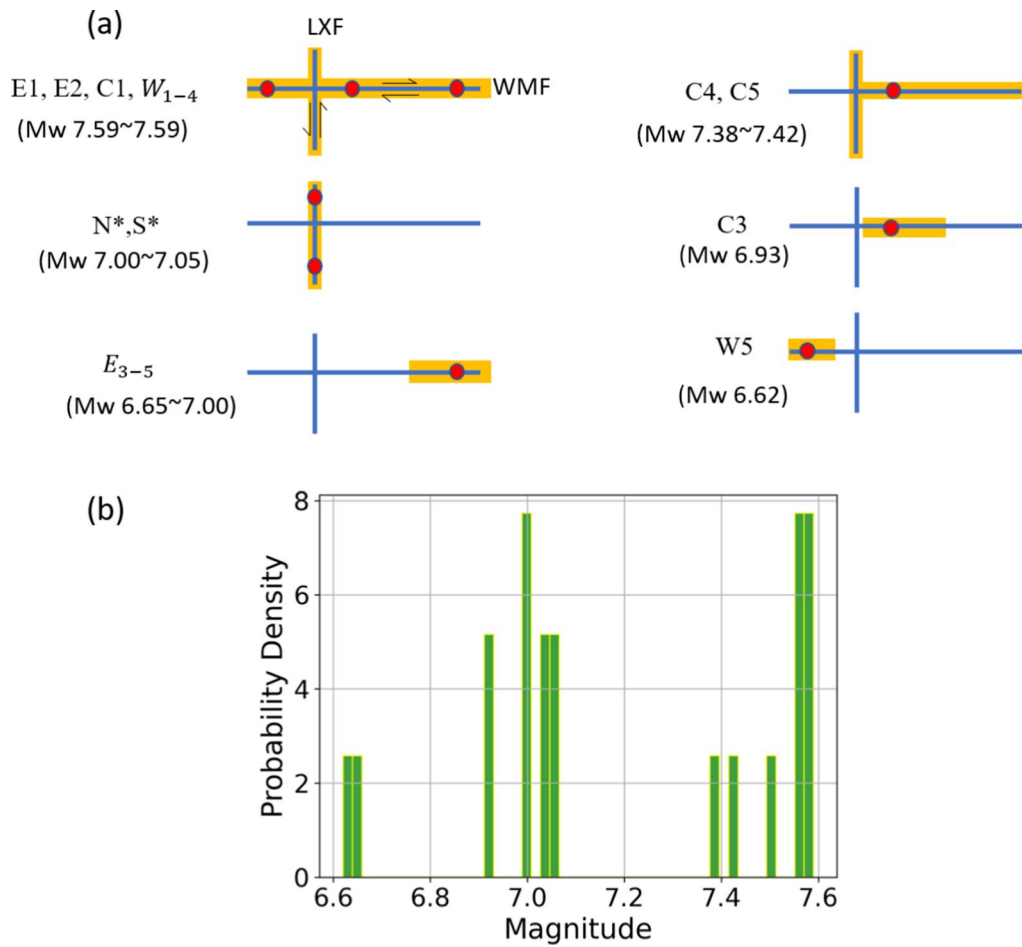
Fig. 10 Slip patterns from all models using simple schematic diagrams **a** and histogram of the magnitudes (M_w) obtained in the 20 simulations **b**. Yellow highlighting indicates the path of propagating rupture, and solid red circles denote the nucleation sites

the free surface amplify the motions of the reverse fault near the free surface. Therefore, reverse faults tend to slip more than strike-slip faults, even in relatively lower stress conditions.

Rupture directivity effects caused by different nucleation positions lead to a prominent spatial difference, confirmed by surface displacements and PGV (Additional file 1: Text S4). The site toward which the rupture front propagates will suffer stronger ground motions than the site where the rupture propagates away due to the cumulative effect of the seismic radiation called forward directivity (Somerville et al. 1997). We further evaluate the strong ground motion and surface offset in Additional file 1: Text S4.

Discussion

We explored several large earthquake scenarios. However, the dynamic rupture propagation results depend on several key factors, including the initial stress, fault geometry, frictional parameters, and hypocenters, which might
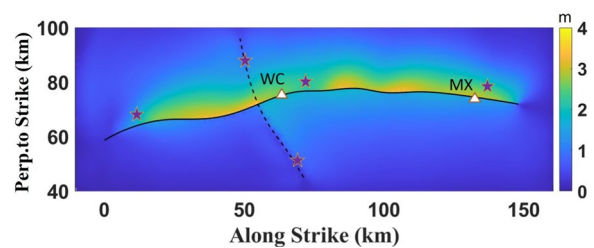

Fig. 11 The map for maximum surface displacements from 20 simulations. The white triangles present the two main cities (Wenchuan and Maoxian) and red stars denote the epicenters

lead to large uncertainty for different earthquake scenarios. For instance, different cases with a linear increase in stress from the surface down to some specified saturation depth might result in different ground motion distributions. We include this uncertainty by changing the specified depth but lowering the maximum stress, so that the same average stress drop can be maintained for the

two cases (Fig. 9). Without loss of generality, we model 20 scenarios of dynamic rupture propagations (Table 1) to investigate the effects of neighboring parameter space, including μ_d (0.12–0.15) (Yao et al. 2013), D_c (0.8–1.2 m) (Tang et al. 2021b), and the stress saturation depth.

Effect of saturation depth of stress

The average stress drops on the WMF and LXF are obtained from observations from the 2008 Wenchuan earthquake, but the distribution of stresses along the depth is poorly constrained. The magnitude of the principal vertical stress depends on the overburden pressure (density and depth), which might also be compensated for with increased pore pressure (Hardebeck and Okada 2018). Thus, we build two depth-dependent shear and normal stress regimes with the same average stress drop $\Delta\sigma_w = 2.9$ MPa. The result of the first case has been discussed in the result section. However, the second case leads to different earthquake scenarios and distributions of the coseismic slip (Fig. 9). For the second case with deeper saturation depths, simulated ruptures starting in the east or center of the WMF propagate to 20 km beyond the nucleation area and arrest at the patch where the normal stress is stronger (Additional file 1: Fig. S4). Furthermore, the rupture from the west part propagates over the WMF and cascades to the LXF but leads

to a lower magnitude (Table 1) and coseismic slips than that of W1 (Fig. 8). However, unlike the scenarios on the oblique fault (the WMF), the coseismic slip and magnitudes on the sinistral fault (the LXF) are slightly larger than that in case 1. These phenomena suggest that depth-dependent stress patterns might affect dip-slip faults more than strike-slip faults, and a larger stress gradient near the free surface of an oblique-slip fault is more likely to trigger a stronger coseismic slip.

Patterns of ruptures in the WMF and LXF fault systems

The earthquake scenarios from all simulations in Table 1 can be summarized as six patterns (Fig. 10a). The 20 cases evaluated do not cover the entire range of possibilities, and the assigned probabilities remain arbitrary, because the uncertainty of the geometry and initial stress is not fully considered. However, the proposed scenarios in this study are understandable from a mechanics standpoint; therefore, they appear possible. The spatial heterogeneity introduced in this study originates from fault geometry and inverted regional stress, which principally controls the macroscopic patterns. For instance, cascading ruptures jump from oblique to strike-slip faults, but the reverse process is less likely. The ruptures are arrested on the WMF, whereas they easily run through the entire LXF (Fig. 10a). Furthermore, a rupture propagating
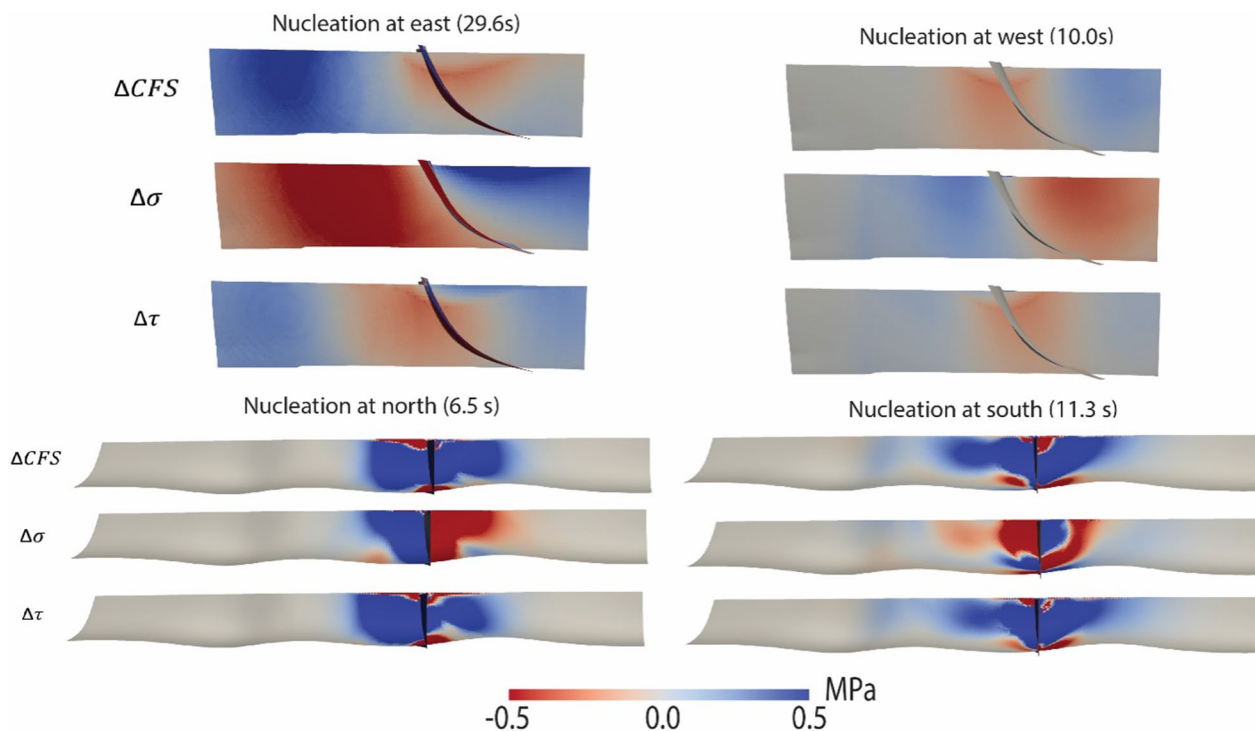

Fig. 12 Stress change near the fault intersection when rupture is approaching. Coulomb-failure stress $\Delta CFS(t) = \Delta\tau(t) - \mu_s \Delta\sigma(t)$, where $\Delta\tau$ is shear stress change, $\Delta\sigma$ normal stress change, and μ_s is static frictional coefficient

eastward causes greater coseismic displacements than westward propagation.

Figure 10b represents a statistical analysis of the moment magnitude based on the deterministic simulation results. The earthquake scenarios fall into three groups: magnitudes of approximately 7.5, 7.0, or near 6.6. The first group includes earthquakes that start on the WMF and can propagate over all or most parts of the two faults. Earthquakes with magnitudes of approximately 7.0 typically come from the LXF or local ruptures on the WMF. The third group includes earthquakes that start on the WMF but quickly stop near the nucleation patch due to the unfavorable fault orientation because of the friction parameters and on-fault stress.

Incorporating all earthquake scenarios to further assess the potential seismic motion, we calculate the maximum surface displacements shown in Fig. 11. Static surface deformation is crucial for near-source hazard analyses. Figure 11 shows the two prominent peaks at 40 km and 100 km along-strike distances. Wenchuan town is near the edge of the moderate slip, and Maoxian town is in the extent of the larger slip. The PGV distributions (Additional file 1: Text S4) indicate moderately higher values of PGV around Maoxian than Wenchuan when a rupture nucleates at the center or eastern end of the WMF. The velocity structures,

including site conditions, are not included in these simulations; therefore, the results for ground shaking from an actual earthquake, even if it were the same source as shown in these simulations, would differ significantly due to the structural effects.

Furthermore, the values of $\mu_d = 0.12$–0.15 are slightly lower than those used in Wenchuan earthquake simulations ($\mu_d = 0.18$) (Zhang et al. 2019; Tang et al. 2021b). Suppose the same friction parameters are used in this study, ruptures will be challenging to initiate in the designed nucleation zone, because relative strength parameter S (Bizzarri et al. 2011) will be larger. Besides, the steeper dip angle near the surface of the WMF (Fig. 6) tends to increase the normal stress, enhancing the fault clamping effect and making it more difficult to slip. Thus, if our model of the WMF with a steeper dip angle is correct, the WMF will be more stable than the BCF in the long term.

Explanation of rupture patterns

We simulated large earthquake scenarios (models E1–C1). Two interesting scientific issues are worthy of further discussion. First, why do cascading ruptures jump from oblique to strike-slip faults, but the reverse process is challenging? Second, why does the eastward rupture cause greater coseismic displacements than the westward
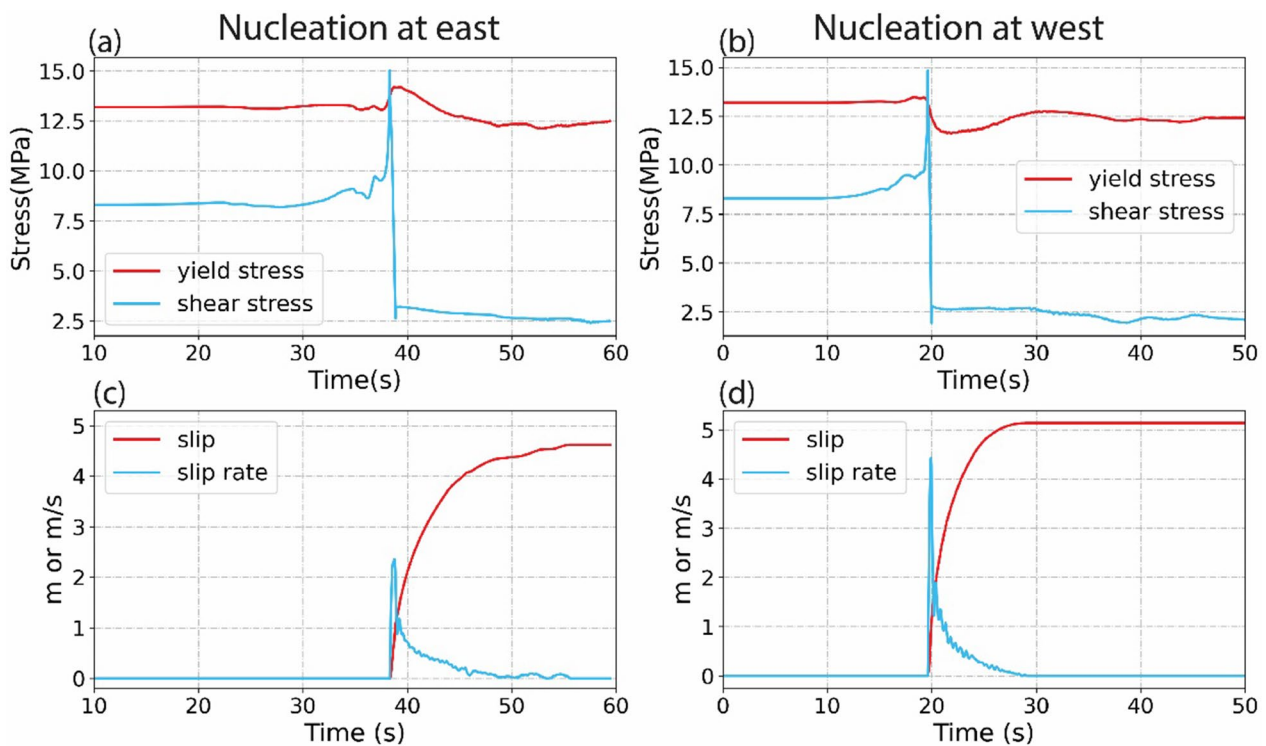

Fig. 13 Evolution of stress and slip for the cases with different nucleation positions. The location of fault point is indicated in Fig. 8

propagation? Although we have mentioned that the rupture directivity can answer the second question, we hope to further explore the deeper reasons from a mechanics perspective.

We answer the first question by calculating the shear stress changes $\Delta\tau$, normal stress change $\Delta\sigma$ (positive in compression), and the ΔCFS on the two faults under the state when a rupture is approaching the fault intersection (Fig. 12). The ΔCFS is calculated from $\Delta CFS = \Delta\tau - \mu_s \Delta\sigma$ (King et al. 1994; Harris 1998), measuring whether the fault is brought closer or farther from failure after slip on an adjacent fault (Freed 2005; Parsons et al. 2008; Liu et al. 2018). Ruptures nucleating at the east or west ends of the WMF approach the fault intersection and induce a positive ΔCFS on the LXF. The primary contribution of the increase in ΔCFS comes from $\Delta\tau$ rather than $\Delta\sigma$, although the normal stress change affects a larger area of the LXF. On the other hand, simulated ruptures nucleating at the north or south ends of the LXF approach the fault intersection and can induce a negative ΔCFS on the WMF. The ΔCFS in most areas near the intersection of the WMF is negative, although there are small-scale positive ΔCFS locally.

The fault activity depends on its prestress state besides the ΔCFS. However, it is more challenging to observationally determine the absolute prestress level or when in its seismic cycle than the principal stress orientation and the stress ratio. The prediction can be more complicated if we consider further stress heterogeneity than those in our modeling. With such a limitation, the LXF has higher initial shear stress than the WMF (Additional file 1: Fig. S4); therefore, the LXF will be closer to failure than the WMF. Consequently, with the evolution of the ΔCFS of the four cases, it is reasonable to expect the cascading ruptures to jump from oblique to strike-slip faults rather than the reverse.

We now answer the second question: Why does the eastward rupture cause greater coseismic slips than the westward propagation? We emphasize that all conditions in the two cases are the same except for the different nucleation positions or rupture propagating directivity. The increase in the coseismic slip is distributed over most of the fault rather than a local area, meaning that the stress evolution at a specific point (the point shown in Fig. 8) on the fault might help reveal the physical mechanism of this phenomenon (Fig. 13). The shear stress variations are similar in the two cases, and the dynamic stress drops are the same. However, the normal stress suddenly increases when the rupture propagates from east to west (Fig. 13a). The seismic waves generated by the rupture superimpose on the edge of the rupture front and couple with the hanging wall moving in the opposite direction (oblique and dextral slip), forming a local compression.

This transient increase in normal stress weakened the slip rate to reach a large peak value (Fig. 13c), resulting in a lower coseismic slip than that of reverse propagating directivity. Our results correlate with the study by Tang et al. (2021a).

Conclusions

We developed a new algorithm based on the Wallace–Bott hypothesis for the inversion of fault geometry to infer nonplanar fault geometry in the Wenchuan region. Without sufficient geophysical or geological data to constrain the fault geometry, this is an effective scheme to refine fault geometry with long-term slip-rate data.

Combining deterministic simulations of earthquake dynamics, we assessed the rupture scenarios expected from the present stress field and given the fault geometry of the WMF and LXF. Areas of large ground motion largely depend on where the earthquake nucleates. Several fault nucleation points, friction coefficients, and initial stress states were evaluated, and the general rupture patterns for these earthquake scenarios could fall into three groups. Depending on the initial conditions, the dynamic rupture might start in the LXF, leading to magnitude-7.0 earthquakes, or start in the WMF, then cascade through the LXF, leading to magnitude-7.5 earthquakes, or both start and arrest in the WMF, leading to magnitude-6.5 or -7.0 earthquakes. We limited the extent of faults based on available surface fault data, and the maximum magnitudes of future earthquakes can be more significant if faults not in this model interact.

Furthermore, we find the general tendencies of a reverse oblique fault with a conjugate strike-slip fault. Due to the positive ΔCFS near the fault intersection, a rupture starting on the reverse oblique-slip jumps to the strike-slip fault. However, the reverse process is challenging, because the negative ΔCFS dominates near the intersection. Furthermore, the ground motion might be enhanced if the rupture propagation direction is consistent with the movement direction of the hanging wall, because a local decrease of normal stress enhances the coseismic slip.

While we applied our new systematic and physically based method to the case of WMF/LXF, this would apply to any other fault systems in the world where available data are limited to develop models. Therefore, we expect this method to be further tested in other cases and to be able to contribute to the assessment of future earthquake scenarios.

Supplementary Information

Additional file 1: Text S1. Stress inversion. **Text S2.** Test on parameters for fault geometry inversion. **Text S3.** The effect from Wenchuan mainshock . **Appendix A.** Conjugate gradient method for fault geometry inversion. **Text S4**. Peak ground displacement and velocity. **Figure S1**. Map showing the setting of major faults of the center Longmen Shan fault zone. The red bold black lines indicate the field-confirmed rupture traces in Wenchuan earthquake (Xu et al. 2009; Liu-Zeng et al. 2009). The blue solid and dotted lines represent the WMF and Lixian faults, both of which did not slip in the main shock but are very active in aftershocks. Accurate fault trace of the WMF is from the field investigation by Xie et al (2011), and the location of the LXF trace is from the distribution of aftershocks (Yin et al. 2018; Li et al. 2019). "Beach ball" represents the lower hemisphere projection of the focal mechanism (strike 225°/dip 39°/rake 120°) of the $M_w7.9$ ($M_s8.0$) Wenchuan earthquake obtained from Zhang (2009). Pink circles—historic strong earthquakes (Before 2008) larger than M5. Yellow circles— historic strong earthquakes (Before 2008) with magnitude $4 \leq M < 5$. The white arrow indicates block motion direction. CD— Chengdu; DY—Dayi; YX—Yingxiu; WC—Wenchuan; LX—Lixian; MX— Maoxian; BC—Beichuan; NB—Nanba. **Figure S2**. Seismicity following the 2008 Wenchuan earthquake plotted in the along-strike distances (**a**) and cross-section along the purple box (**b**). **Figure S3**. Boundary elements for each fault segment and free surface. We employed the boundary elements of approximately 26,824, and control triangular elements to be 500 m on the fault and free surface in the vicinity of the fault, and increase this size with a maximum rate of 7.5 times toward the outer boundary of the surface until it reaches the maximum size of around 2000 m. **Figure S4.** Initial on-fault shear stress and normal stress resolved by the tectonic stress, as well as Initial on-fault shear stress drop $\tau_{drop} = \tau_0 - \mu_d \sigma$, $\mu_d = 0.12$. **Figure S5. a** The spatial distribution of 391 focal mechanism solutions (beachball, lower hemisphere stereographic projection) determined in this study from earthquakes between 2009 and 2016. The color and size of the beachballs indicate the type and seismic moment, respectively. Red, normal (NF) or normal oblique faulting (NS); green, strike-slip faulting (SS); blue, thrust (TF) or thrust oblique faulting (TS); black, mixed type. **b** Histogram illustrating the faulting type distribution of the earthquake focal mechanism data determined in this study. (From Li et al. 2019). **Figure S6.** Inferred regional stress field. **a** The trade-off between model length and data misfit, $e = 1.6$ is selected to be the optimal damping parameter. **b** An example to show the distribution of Closeness between best stress tensor and inverted stress tensors from 1000 times bootstraps in grid number 1. To estimate the stress uncertainty with 95% confidence, we pick 95% of them that have the highest scalar product with the best stress tensor. **c** Results of crustal stress field inversion from 440 fault plane solutions for the Longmen Shan region with a grid interval of 0.2° both in longitude and latitude (only the stresses in our calculation domain are shown). **d** The principal stress axes obtained in each block are denoted by red (σ_1), blue (σ_2) and green (σ_3) in the lower hemisphere stereonet. **Figure S7.** Along strike distribution of scaled three-component principal stress. The scaled three-component principal stress are marked red (σ_1), blue (σ_2) and green (σ_3) colors, which are derived using bootstrap resampling of the selected fault planes. The black circles denote the stress component closest to the vertical, and the dotted lines are the average of each stress component (**a**). The orange solid line and red dash line represent the trend and average of principal stress orientation (**b**). **Figure S8.** Inversions of fault geometry with different horizontal intervals of interpolated curves. From top to bottom: Observed long-term slip rates and scaled traction; Distribution of inverted parameters η; Objective functions versus iterations; Final fault surface derived from inverted parameters η. Other details for each plot refer to Fig. 4. **Figure S9.** Same as Additional file 1: Fig. S7, but with different integral radius. **Figure S10.** Same as Additional file 1: Fig. S7, but with regularization parameters. **Figure S11. a** Calculated Coulomb failure stress change and the movement of Lixian Fault, assuming $\mu_s = 0.52$ (Modified from Tang et al. 2021a, b). The spatial distribution of aftershocks is from Yin et al. (2018). **b** The Coulomb stress change of the WMF, assuming that the LXF ruptures at southern end. **Figure S12.** Three components and magnitude of surface slip, with eastern and western nucleation points. The white pentagrams denote the epicenter. The white arrow indicates the NE direction. See Fig. 5 for the definition of the x-y-z components. **Figure S13.** Magnitude of peak ground velocities from different nucleation points. The white pentagrams denote the epicenter. **Figure A1**. Schematic to describe the calculation of traction from interpolated fault surface. Green circles are the control points at equal intervals on the dip curves, and orange circles denote the equally spaced points on the interpolation curves. The average interval of collocation points is around 3 km. The inverted triangles represent the locations of the measured points.

Availability of data and materials

Acknowledgement for the data support from China Earthquake Networks Center, National Earthquake Data Center (https://data.earthquake.cn/). Videos in this paper can be downloaded from https://zenodo.org/record/7077841#.YyGRFnZBxD8. The simulation data and code used in this study are available from the corresponding author upon request.

Declarations

Ethics approval and consent to participate
Not applicable.

Consent for publication
Not applicable.

Competing interests
The authors declare that they have no competing interests.

Author details
[1]Yangtze Delta Region Institute of University of Electronic Science and Technology of China, Huzhou, Zhejiang, China. [2]Department of Earth and Planetary Science, School of Science, University of Tokyo, Bunkyō, Tokyo, Japan.

References

Abrahamson NA, Somerville PG (1996) Effects of the hanging wall and footwall on ground motions recorded during the Northridge earthquake. Bull Seismol Soc Am 86(1B):S93–S99

Anderson EM (1905) The dynamics of faulting. Trans Edinburgh Geol Soc 8(3):387–402

Ando R (2016) Fast domain partitioning method for dynamic boundary integral equations applicable to non-planar faults dipping in 3-D elastic half-space. Geophys J Int 207(2):833–847

Ando R, Kaneko Y (2018) Dynamic rupture simulation reproduces spontaneous multifault rupture and arrest during the 2016 Mw 7.9 Kaikoura earthquake. Geophysical Res Lett. https://doi.org/10.1029/2018GL080550

Ando R, Okuyama S (2010) Deep roots of upper plate faults and earthquake generation illuminated by volcanism. Geophys Res Lett. https://doi.org/10.1029/2010GL042956

Ando R, Imanishi K, Panayotopoulos Y, Kobayashi T (2017) Dynamic rupture propagation on geometrically complex fault with along-strike variation of fault maturity: insights from the 2014 Northern Nagano earthquake. Earth Planets Space. https://doi.org/10.1186/s40623-017-0715-2

Andrews DJ (1976) Rupture velocity of plane strain shear cracks. J Geophys Res 81(32):5679–5687

Aochi H, Fukuyama E (2002) Three-dimensional nonplanar simulation of the 1992 Landers earthquake. J Geophy Res Solid Earth 107(B2):ESE-4

Aochi H, Ulrich T (2015) A probable earthquake scenario near Istanbul determined from dynamic simulations. Bull Seismol Soc Am 105(3):1468–1475

Asano K, Iwata T (2016) Source rupture processes of the foreshock and mainshock in the 2016 Kumamoto earthquake sequence estimated from the kinematic waveform inversion of strong motion data. Earth Planets Space 68(1):1–11

Bizzarri A (2011) On the deterministic description of earthquakes. Rev Geophys. https://doi.org/10.1029/2011RG000356

Bott MH (1959) The mechanics of oblique slip faulting. Geol Mag 96(2):109–117

Densmore AL, Ellis MA, Li Y, Zhou R, Hancock GS, Richardson N (2007) Active tectonics of the Beichuan and Pengguan faults at the eastern margin of the Tibetan Plateau. Tectonics. https://doi.org/10.1029/2006TC001987

Duan B (2010) Role of initial stress rotations in rupture dynamics and ground motion: a case study with implications for the Wenchuan earthquake. J Geophys Res Solid Earth. https://doi.org/10.1029/2009JB006750

Elliott AJ, Oskin ME, Liu-Zeng J, Shao Y (2015) Rupture termination at restraining bends: the last great earthquake on the Altyn Tagh Fault. Geophys Res Lett 42:2164–2170

Feng G, Jónsson S, Klinger Y (2017) Which fault segments ruptured in the 2008 Wenchuan earthquake and which did not? New evidence from near-fault 3D surface displacements derived from SAR image offsets. Bull Seismol Soc Am 107(3):1185–1200

Freed AM (2005) Earthquake triggering by static, dynamic, and postseismic stress transfer. Annu Rev Earth Planet Sci 33:335–367

Fukahata Y, Hashimoto M (2016) Simultaneous estimation of the dip angles and slip distribution on the faults of the 2016 Kumamoto earthquake through a weak nonlinear inversion of InSAR data. Earth Planets Space 68(1):1–10

Hardebeck JL, Michael AJ (2006) Damped regional-scale stress inversions: Methodology and examples for southern California and the Coalinga aftershock sequence. J Geophy Res Solid Earth 111(B11):B11310. https://doi.org/10.1029/2005JB004144

Hardebeck JL, Okada T (2018) Temporal stress changes caused by earthquakes: a review. J Geophys Research Solid Earth 123(2):1350–1365

Harris RA (1998) Introduction to special section: Stress triggers, stress shadows, and implications for seismic hazard. J Geophy Res Solid Earth 103:24347–24358

Harris RA (2004) Numerical simulations of large earthquakes: dynamic rupture propagation on heterogeneous faults. Pure Appl Geophys 161(11/12):2171–2181

Harris RA, Barall M, Lockner DA, Moore DE, Ponce DA et al (2021) A geology and geodesy based model of dynamic earthquake rupture on the Rodgers Creek-Hayward-Calaveras fault system, California. J Geophys Res Solid Earth 126(3):e2020JB020577

Hok S, Fukuyama E (2011) A new BIEM for rupture dynamics in half-space and its application to the 2008 Iwate-Miyagi Nairiku earthquake. Geophys J Int 184(1):301–324

Hubbard J, Shaw JH, Klinger Y (2010) Structural setting of the 2008 Mw 7.9 Wenchuan, China, earthquake structural setting of the 2008 Mw 7.9 Wenchuan, China, earthquake. Bull Seismol Soc Am 100(5B):2713–2735

Imanishi K, Ando R, Kuwahara Y (2012) Unusual shallow normal-faulting earthquake sequence in compressional northeast Japan activated after

the 2011 off the Pacific coast of Tohoku earthquake. Geophysical Res Lett 39(9):100. https://doi.org/10.1029/2012GL051491

Jia D, Li Y, Lin A, Wang M, Chen W et al (2010) Structural model of 2008 Mw 7.9 Wenchuan earthquake in the rejuvenated Longmen Shan thrust belt, China. Tectonophysics 491(1–4):174–184

Kanamori H, Anderson DL (1975) Theoretical basis of some empirical relations in seismology. Bull Seismol Soc Am 65(5):1073–1095

King GC, Stein RS, Lin J (1994) Static stress changes and the triggering of earthquakes. Bull Seismol Soc Am 84(3):935–953

Lejri M, Maerten F, Maerten L, Soliva R (2015) Paleostress inversion: a multiparametric geomechanical evaluation of the Wallace-Bott assumptions. Tectonophysics 657:129–143

Li Y, Jia D, Shaw JH, Hubbard J, Lin A et al (2010) Structural interpretation of the coseismic faults of the Wenchuan earthquake: three-dimensional modeling of the Longmen Shan fold-and-thrust belt. J Geophys Res Solid Earth. https://doi.org/10.1029/2009JB006824

Li X, Hergert T, Henk A, Wang D, Zeng Z (2019) Subsurface structure and spatial segmentation of the Longmen Shan fault zone at the eastern margin of Tibetan Plateau: evidence from focal mechanism solutions and stress field inversion. Tectonophysics 757:10–23

Lisle RJ (2013) A critical look at the Wallace-Bott hypothesis in fault-slip analysis. Bulletin De La Société Géologique De France 184(4–5):299–306

Liu Z, Liang C, Hua Q, Li Y, Yang Y et al (2018) The seismic potential in the seismic gap between the Wenchuan and Lushan earthquakes revealed by the joint inversion of receiver functions and ambient noise data. Tectonics 37:4226–4238

Liu-Zeng J, Zhang Z, Wen L, Tapponnier P, Sun J et al (2009) Coseismic ruptures of the 12 May 2008, Ms 80 Wenchuan earthquake, Sichuan East–west crustal shortening on oblique, parallel thrusts along the eastern edge of Tibet. Earth Planet Sci Lett 286(3–4):355–370

Lu R, He D, John S, Wu JE, Liu B, Chen Y (2014) Structural model of the central Longmen Shan thrusts using seismic reflection profiles: Implications for the sediments and deformations since the Mesozoic. Tectonophysics 630:43–53

Luna LM, Hetland EA (2013) Regional stresses inferred from coseismic slip models of the 2008 Mw 7.9 Wenchuan, China, earthquake. Tectonophysics 584:43–53

Ma S, Beroza GC (2008) Rupture dynamics on a bimaterial interface for dipping faults. Bull Seismol Soc Am 98(4):1642–1658

Ma B, Su G, Hou Z, Shu S (2005) Late quaternary slip rate in the central part of the Longmen Shan fault zone from terrace deformation along the Minjiang River. Seismology and Geology 27(2):234–242

Matsumoto S, Yamashita Y, Nakamoto M, Miyazaki M, Sakai S et al (2018) Prestate of stress and fault behavior during the 2016 Kumamoto earthquake (M7. 3). Geophys Res Lett 45(2):637–645

McKinley S, Levine M (1998) Cubic spline interpolation. Coll Redwoods 45(1):1049–1060

Michael AJ (1984) Determination of stress from slip data: faults and folds. J Geophys Res Solid Earth 89(B13):11517–11526

Mikumo T, Olsen KB, Fukuyama E, Yagi Y (2003) Stress-breakdown time and slip-weakening distance inferred from slip-velocity functions on earthquake faults. Bull Seismol Soc Am 93(1):264–282

Oglesby DD (2005) The dynamics of strike-slip step-overs with linking dip-slip faults. Bull Seismol Soc Am 95(5):1604–1622

Oglesby DD, Mai PM (2012) Fault geometry, rupture dynamics and ground motion from potential earthquakes on the North Anatolian Fault under the Sea of Marmara. Geophys J Int 188(3):1071–1087

Oglesby DD, Archuleta RJ, Nielsen SB (2000) The three-dimensional dynamics of dipping faults. Bull Seismol Soc Am 90(3):616–628

Parsons T, Ji C, Kirby E (2008) Stress changes from the 2008 Wenchuan earthquake and increased hazard in the Sichuan basin. Nature 454(7203):509–510

Pei S, Su J, Zhang H, Sun Y, Toksöz MN et al (2010) Three-dimensional seismic velocity structure across the 2008 Wenchuan Ms 8.0 earthquake, Sichuan, China. Tectonophysics 491(1–4):211–217

Qin X, Chen Q, Wu M, Tan C, Feng C, Meng W (2015) In-situ stress measurements along the Beichuan-Yingxiu fault after the Wenchuan earthquake. Eng Geol 194:114–122

Ramirez-Guzman L, Hartzell S (2020) 3-D joint geodetic and strong-motion finite fault inversion of the May 12, 2008, Wenchuan. China Earthquake Geophys J Int 222(2):1390–1404

Ramos MD, Huang Y, Ulrich T, Li D, Gabriel AA, Thomas AM (2021) Assessing margin-wide rupture behaviors along the Cascadia megathrust with 3-D dynamic rupture simulations. J Geophys Res Solid Earth 126(7):e2021JB022005

Ramos MD, Thakur P, Huang Y, Harris RA, Ryan K (2022) Working with dynamic earthquake rupture models: a practical guide. Seism Res Lett 93(4):2096–2110

Ran YK, Chen WS, Xu XW, Chen LC, Wang H, Yang CC, Dong SP (2013) Paleoseismic events and recurrence interval along the Beichuan-Yingxiu fault of Longmenshan fault zone, Yingxiu, Sichuan, China. Tectonophysics 584:81–90

Rice JR (1992) Fault stress states, pore pressure distributions, and the weakness of the San Andreas fault. Int Geophys 51:475–503

Rice JR (1993) Spatio-temporal complexity of slip on a fault. J Geophys Res 98(B6):9885–9907

Rongjun Z, Yong L, Densmore AL, Ellis MA, Yulin H, Yongzhao L, Xiaogang LI (2007) Active tectonics of the Longmen Shan region on the eastern margin of the Tibetan plateau. Acta Geologica Sinica-English Edition 81(4):593–604

Shen ZK, Sun J, Zhang P, Wan Y, Wang M, Bürgmann R et al (2009) Slip maxima at fault junctions and rupturing of barriers during the 2008Wenchuan earthquake. Nat Geosci 10:718–724

Shen X, Tian Y, Zhang G, Zhang S, Carter A, Kohn B et al (2019) Late Miocene hinterland crustal shortening in the Longmen Shan thrust belt, the eastern margin of the Tibetan Plateau. Journal of Geophysical Research: Solid Earth 124(11):11972–11991

Shi B, Anooshehpoor A, Brune JN, Zeng Y (1998) Dynamics of thrust faulting: 2D lattice model. Bull Seismol Soc Am 88(6):1484–1494

Somerville PG, Smith NF, Graves RW, Abrahamson NA (1997) Modification of empirical strong ground motion attenuation relations to include the amplitude and duration effects of rupture directivity. Seismol Res Lett 68(1):199–222

Tan XB, Xu XW, Lee YH, Lu RQ, Liu Y et al (2017) Late Cenozoic thrusting of major faults along the central segment of Longmen Shan, eastern Tibet: evidence from low-temperature thermochronology. Tectonophysics 712:145–155

Tang RC (1991) The Quaternary activity characteristics of several major active faults in the Songpan-Longmenshan region. Earthquake Res China 7:64–71

Tang R, Yuan J, Gan L (2021a) Free-surface-induced supershear transition in 3-D simulations of spontaneous dynamic rupture on oblique faults. Geophys Res Lett 48(3):e2020GL091621

Tang R, Zhu S, Gan L (2021b) Dynamic rupture simulations of the 2008 79 Wenchuan earthquake: Implication for heterogeneous initial stress and complex multifault geometry. J Geophys Res Solid Earth 126(12):e2021JB022457

Tian Y, Kohn BP, Gleadow AJ, Hu S (2013) Constructing the Longmen Shan eastern Tibetan Plateau margin: Insights from low-temperature thermochronology. Tectonics 32(3):576–592

Tian T, Zhang J, Liu T, Jiang W, Zhao Y (2017) Morphology, tectonic significance, and relationship to the Wenchuan earthquake of the Xiaoyudong Fault in Western China based on gravity and magnetic data. J Asian Earth Sci 138:672–684

Tikhonov AN (1963) On the solution of ill-posed problems and the method of regularization. Russian Academy of Sciences 151(3):501–504

Tong P, Yang D, Huang X (2019) Multiple-grid model parametrization for seismic tomography with application to the San Jacinto fault zone. Geophys J Int 218(1):200–223

Ulrich T, Gabriel AA, Ampuero JP, Xu W (2019) Dynamic viability of the 2016 Mw 7.8 Kaikōura earthquake cascade on weak crustal faults. Nature Commun 10(1):1–16

Wallace RE (1951) Geometry of shearing stress and relation to faulting. J Geol 59:118–130

Wan Y, Shen ZK, Bürgmann R, Sun J, Wang M (2016) Fault geometry and slip distribution of the 2008 Mw 7.9 Wenchuan, China earthquake, inferred from GPS and InSAR measurements. Geophys J Int 208(2):748–766

Wang H, Chen L, Ran Y, Lei S, Li X (2015) Paleoseismic investigation of the seismic gap between the seismogenic structures of the 2008 Wenchuan and 2013 Lushan earthquakes along the Longmen Shan fault zone at the eastern margin of the Tibetan Plateau. Lithosphere 7:14–20

Wang C, Liang C, Deng K, Huang Y, Zhou L (2018) Spatiotemporal distribution of microearthquakes and implications around the seismic gap between the Wenchuan and Lushan earthquakes. Tectonics 37:2695–2709

Wang Z, Wang J, Yang X (2021) The role of fluids in the 2008 Ms 8.0 Wenchuan earthquake. J Geophys Res Solid Earth 126:e2020JB019959

Wu JP, Huang Y, Zhang TZ, Ming YH, Fang LH (2009) Aftershock distribution of the MS8. 0 Wenchuan earthquake and 3D P-wave velocity structure in and around source region. Chinese J Geophys 52(1):102–111

Xie XS, Jiang WL, Feng XY (2011) Discussion appearance of surface fractures along the rear-range of Longmenshan mountain during 2008 Ms8.0 Wenchuan earthquake. Acta Seismol Sin 33(1):62–81

Xu X, Wen X, Yu G, Chen G, Klinger Y et al (2009) Coseismic reverse-and oblique-slip surface faulting generated by the 2008 Mw 79 Wenchuan earthquake, China. Geology 37(6):515–518

Yang N, Zhang YQ (2010) Tission-track dating for activity of the Longmenshan fault zone and uplifting of the western Sichuan Plateau. J Geomech 16(4):359–371

Yang H, Liu Y, Lin J (2013) Geometrical effects of a subducted seamount on stopping megathrust ruptures. Geophys Res Lett 40:1–6

Yao S, Yang H (2022) Hypocentral dependent shallow slip distribution and rupture extents along a strike-slip fault. Earth Planet Sci Lett 578:117296

Yao L, Ma S, Shimamoto T, Togo T (2013) Structures and high-velocity frictional properties of the Pingxi fault zone in the Longmenshan fault system, Sichuan, China, activated during the 2008 Wenchuan earthquake. Tectonophysics 599:135–156

Yin XZ, Chen JH, Peng Z, Meng X, Liu QY et al (2018) Evolution and distribution of the early aftershocks following the 2008 Mw 7.9 Wenchuan earthquake in Sichuan, China. J Geophys Res Solid Earth 123(9):7775–7790

Zhang Y, Wang R, Zschau J, Chen YT, Parolai S, Dahm T (2014) Automatic imaging of earthquake rupture processes by iterative deconvolution and stacking of high-rate GPS and strong motion seismograms. J Geophys Res Solid Earth 119(7):5633–5650

Zhang Z, Zhang W, Chen X, Li PE, Fu C (2017) Rupture dynamics and ground motion from potential earthquakes around Taiyuan, China. Bull Seismol Soc Am 107(3):1201–1212

Zhang Z, Zhang W, Chen X (2019) Dynamic rupture simulations of the 2008 Mw7.9 Wenchuan earthquake by the curved grid finite-difference method. J Geophys Res Solid Earth 124(10):10565–11058

Zhao B, Shi Y, Gao Y (2011) Relocation of aftershocks of the Wenchuan M S 8.0 earthquake and its implication to seismotectonics. Earthq Sci 24(1):107–113

Zhao G, Unsworth MJ, Zhan Y, Wang L, Chen X et al (2012) Crustal structure and rheology of the Longmenshan and Wenchuan Mw 7.9 earthquake epicentral area from magnetotelluric data. Geology 40(12):1139–1142

Publisher's Note